

Loschmidt-amplitude wave function spectroscopy and the physics of dynamically driven phase transitions

D.M. Kennes,¹ C. Karrasch,¹ and A.J. Millis^{2,3}

¹*Dahlem Center for Complex Quantum Systems and Fachbereich Physik,
Freie Universität Berlin, 14195 Berlin, Germany*

²*Department of Physics, Columbia University, 538 West 120th Street, New York, NY 10027 USA*

³*Center for Computational Quantum Physics, Flatiron Institute, 162 5th Avenue, New York, NY 10010 USA*

(Dated: June 24, 2022)

We introduce the Loschmidt-amplitude as a powerful tool to perform spectroscopy of generic many-body wave functions. We use our machinery to interrogate the wave function obtained after (one or multiple) Kibble-Zurek ramps within the transverse field quantum Ising model. Known results for the scaling of defects or regarding the preference of the ramp to populate the lowest parts of the multi-magnon bands are confirmed explicitly. We obtain a more complete understanding of the population of defects on the level of the many-body wave function as well as of the effects of magnon-magnon interaction or finite size corrections. We add to the Kibble-Zurek picture the aspect of quantum coherence and its influence on the defect dynamics.

Controlling quantum systems by application of tailored light pulses or other nonequilibrium protocols is established in quantum optics [1] and is rapidly growing in importance in condensed matter physics [2–4]. The goal is to design protocols that change the behavior of a system in some desired way, thereby accessing new regimes of behavior not accessible in equilibrium. Early applications were to few-body systems, but an important current issue is to extend the control to the many-body regime. A crucial issue, more severe in many-body systems than in few-body ones, is that when a system is exposed to an external perturbation, it will in general be excited out of its ground state, so that the distribution function as well as the Hamiltonian changes. Typically, distribution function changes lead after relative short times to quasi-thermal states, in other words to heating the sample, which is often undesirable.

A tailored light field may be thought of as producing a time dependent Hamiltonian $H(t)$. As the time over which H varies becomes longer and longer with respect to the basic energy scales of the system (such as the gap in the excitation spectrum), one expects that with increasing probability the system remains in the instantaneous ground state of the Hamiltonian at time t . Many-body Hamiltonians often exhibit a dense spectrum of levels, making the applicability of these adiabatic-theorem ideas less obvious. One particularly interesting case is the ‘Kibble-Zurek’ situation of a system tuned across a quantum critical point [5–10]. The gap-closing at criticality means that the adiabatic theorem is necessarily violated, leading to creation of excitations whose nature and density depend on the rate at which the system is ramped through criticality.

These simple considerations highlight the need for theoretical methods of assessing the number and nature of the excitations created by a non-equilibrium drive. One way of characterizing a system is wave function spectroscopy: Given a wavefunction $|\Psi\rangle$ at a specific time

t^* , one selects an eigenbasis $|n\rangle$ (e.g., the eigenstates of $H(t = t^*)$) and then constructs the corresponding density matrix $\hat{\rho}$ with elements $\rho_{nm} = \langle n | \Psi \rangle \langle \Psi | m \rangle$. For quantum many-body systems, however, ρ_{nm} cannot be computed straightforwardly due to the prohibitively large size of the Hilbert space.

In this letter, we present a powerful method for analyzing nonequilibrium wave functions which allows one to efficiently determine the spectral content of a given state without explicitly constructing eigenfunctions or finding eigenvalues. Our approach is based on the ‘Loschmidt amplitude’ (squaring to the Loschmidt echo [11]), which is familiar from quantum optics [12, 13] and which has been employed in the pioneering work of Silva [14] to characterize the work done by the application of a nonequilibrium perturbation [15]. We apply the method to the Kibble-Zurek problem of the one dimensional transverse field Ising model tuned through the order-disorder transition, uncovering new results that point to the importance of quantum coherence in Kibble-Zurek physics.

Methods— Consider a closed system described by a wave function $|\Psi(t)\rangle$ which is obtained by the forward time evolution of some initial state $|\Psi_0\rangle$ with respect to a Hamiltonian $H(t)$. Now choose a time t^* and form

$$L(t^*, \omega) = \int_{-\infty}^{\infty} dt' \langle \Psi(t^*) | e^{i(H(t^*) - E_0 - \omega)t'} | \Psi(t^*) \rangle. \quad (1)$$

Writing the integrand in terms of the eigenvalues E_n and eigenstates $|n\rangle$ of $H(t^*)$ gives $L(t^*, \omega) \sim \sum_n |a_n|^2 \delta(\omega - (E_n - E_0))$, where $a_n = \langle n | \Psi(t^*) \rangle$. The Loschmidt amplitude is thus a sum of δ -functions centered at the eigenvalues of the system and with weights determined by the overlap of the given wave function with the eigenfunction in question. If the time integral in Eq. (1) is taken over a finite but large t_{end} , then the δ -peaks are broadened (and one finds the usual Gibbs ringing) and contributions from energetically nearby eigen-

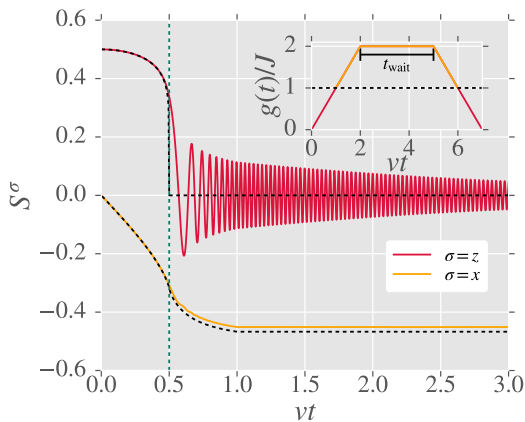


FIG. 1. S^z and S^x for a slow linear ramp through the QCP of the quantum Ising chain ($v/J = 0.02$, $t_{\text{wait}}J \rightarrow \infty$, $g_{\text{end}}/J = 2$, $N \rightarrow \infty$). The dashed green vertical line indicates the time when $g(t) = g_c = 1$. The black dashed curves show the corresponding ground state expectation values with respect to the instantaneous Hamiltonian. Inset: Example of a temporal profile of $g(t)$ which governs the quench ($g_{\text{end}} = 2J$, $v/J = 0.01$, $t_{\text{wait}} = 3/v$). The QCP at $g = g_c = 1$ (dashed black horizontal line) separates the equilibrium ordered phase (red part of $g(t)$) from the disordered phase (orange part of $g(t)$).

states $|n\rangle$ with $E_n \approx E$ contribute to the same peak. In this sense, t_{end} restricts the frequency resolution of the wavefunction spectroscopy. If the spectrum is dense on the scale of this frequency resolution, then $L \sim |a(\omega)|^2 \rho(\omega)$, and we effectively sample the appropriate “state density” $\rho(\omega)$ and corresponding “occupation statistic” $|a(\omega)|^2$.

The key advantage of the Loschmidt amplitude is that the object $e^{i(H(t^*) - E_0 - \omega)t'} |\Psi(t^*)\rangle$ only contains real-time evolutions, which can be calculated efficiently by several methods. Here, we employ the density matrix renormalization group (DMRG), which is an accurate numerical tool to study the equilibrium and non-equilibrium many-body physics of interacting one-dimensional systems. We use a real-time algorithm to directly evaluate Eq. (1) (see Refs. [16–19] as well as the SM). For the model defined below in Eq. (2), we can reach time scales of $Jt_{\text{end}} = 120$ everywhere, which corresponds to a frequency resolution of $\Delta\omega/J \approx 2\pi/240 \approx 0.026$.

Transverse Field Ising Model— As an application, we consider the transverse field Ising model governed by

$$H(J, g) = \sum_{i=1}^{N-1} -J\sigma_i^z \sigma_{i+1}^z + \sum_{i=1}^N g\sigma_i^x, \quad (2)$$

where $\sigma_i^{x,y,z}$ denote Pauli matrices living on site i . At $g = 0$, the ground state of the model spontaneously breaks \mathbb{Z}_2 spin symmetry, yielding long ranged ferromagnetic order with moments aligned to the $\pm z$ direction and a gap to spin excitations. For $0 \leq g \leq J$, the model remains ordered, but the spins begin to cant into the x

direction and the z -component of the magnetization and the excitation gap concomitantly decrease. $g_c = J$ is a quantum critical point with gapless excitations, and for $g > J$ the system is again gapped, with the average spin pointing in the negative x direction.

We briefly review the excitation spectrum [20–22]. The model may be exactly solved; the states are conveniently described [21] in a fermion representation, with the fermion creation operator related to the spin raising operator by a Jordan-Wigner string. At $g > J$ the states are classified into sectors labeled by number of fermions, M . The lowest energy state in a given sector has energy $2M(g - J)$, momentum $k = 0$ and is the M particle filled Fermi sea (note that for a finite system with N sites and periodic boundary conditions the Jordan-Wigner factor shifts momenta so the allowed fermion momenta are odd integers times π/N for even number of particles and even integers times π/N for odd number of particles). Roughly, this ground state corresponds to exciting M $k = 0$ spin waves. The higher energy states in the M particle sector are a continuum of particle-hole excitations above the M particle fermi sea and correspond roughly to exciting $k \neq 0$ spin waves

We now introduce time dependence to the problem: We prepare the system in one of the two $g = 0$ ferromagnetic ground states at time $t = 0$ and for $t > 0$ increases g linearly with a ‘velocity’ v up to value g_{end} greater than unity, then hold g at this value for a waiting time t_{wait} , and eventually decrease it to zero. This ‘double ramp’ is shown in the inset to Fig. 1, and the formal equation for $g(t)$ is given in the SM. We also consider a ‘single ramp’ in which g is increased to a final value and then held indefinitely (by setting $t_{\text{wait}} \rightarrow \infty$).

Single Ramp through QCP— It is instructive to first study the average spin expectation values $S^{x,z} = \langle \sigma_{N/2}^{x,z} \rangle / 2$ for a slow, single ramp through the QCP and $N \rightarrow \infty$ (see Fig. 1). As g is gradually increased away from $g = 0$, at first $S^{x,z}$ remain indistinguishable from the ground state value calculated using the instantaneous Hamiltonian at time t , as expected from the adiabatic theorem [23, 24]. However, when g approaches the critical value $g = 1$ (shown as a vertical dashed line), the adiabatic assumption breaks down; both S^x and S^z begin to deviate from their instantaneous values and for $g > 1$ retain a “footprint” of the QCP-crossing. S^x saturates to a constant value slightly smaller than the ground state one; the difference reflects the density of defects created as the system is tuned through the QCP and goes to zero as the ramp speed decreases. More intriguingly, S^z exhibits coherent oscillations around the equilibrium value $S^z = 0$ which only decay to zero at very long times. Coherent oscillations of the magnetization were not anticipated within the standard Kibble-Zurek arguments, and we now turn to the Loschmidt methods to gain a better understanding of the physics of tuning through a

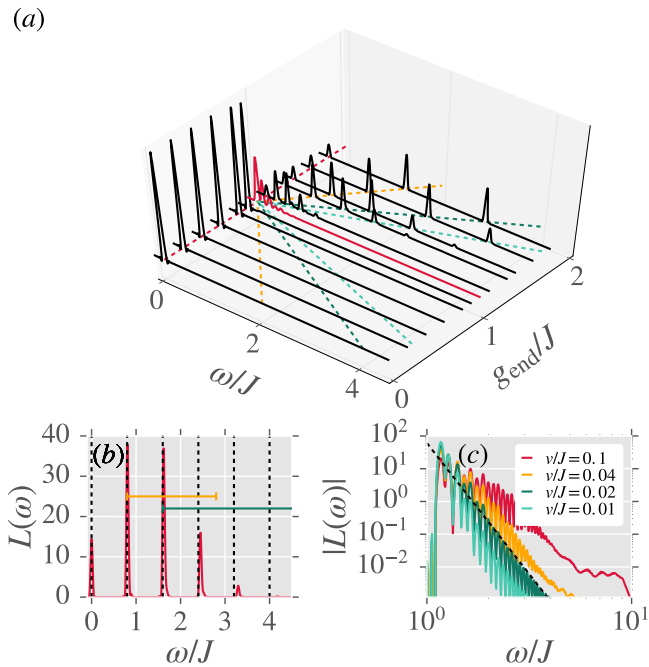


FIG. 2. Wavefunction spectrum $L(\omega)$ for a single forward ramp with $t_{\text{wait}}J \rightarrow \infty$ and $N = 100$. (a) $L(\omega)$ for fixed $v = 0.02J$ and different g_{end} . The evolution is adiabatic for $g_{\text{end}} < g_c = 1$; the spectrum shows a single peak corresponding to the ground state energy $\omega = 0$ (dashed red line). After crossing the QCP, the wavefunction contains a superposition of eigenstates which are strongly localized in energy around integer multiples of the gap $\Delta = 2|g_{\text{end}} - J|$ (colored dashed lines). The slice for $g_{\text{end}} = g_c = J$ is highlighted in red. (b) $L(\omega)$ for fixed $v = 0.02J$ and $g_{\text{end}}/J = 1.4$. Dashed vertical lines indicate $\omega = 2|g_{\text{end}} - J|M$; yellow and green horizontal bars show the width of the first and second magnon band, respectively. (c) $L(\omega)$ for a ramp that stops at the QCP $g_{\text{end}}/J = 1.0$ at different v . The dashed line shows a $\sim t^{-8}$ power-law.

quantum phase transition.

We have computed the Loschmidt amplitude at different points during the evolution of g from $g = 0$ to $g = 2J$. Panel (a) of Fig. 2 summarizes the results, plotting $L(t, \omega)$ against ω for different t (parametrized here by the corresponding value of $g(t)$). For times corresponding to $g(t) < J$, the evolution is adiabatic, and the probability for being in any state except the ground state associated with $g(t)$ is negligible. In the immediate vicinity of the critical point (slice highlighted in red), the spectrum is more complex, with a large number of low energy states excited. For larger $g > 1$, the situation simplifies again, and only a very small number of energies have a non-negligible contribution to the wave function. These states are at energies corresponding closely to integer multiples of the lowest, zero-momentum excitation energy $\Delta = 2|g - J|$ (dashed colored lines) [20–22] (for an analysis of the width of the peaks, which scales with v , see the SM).

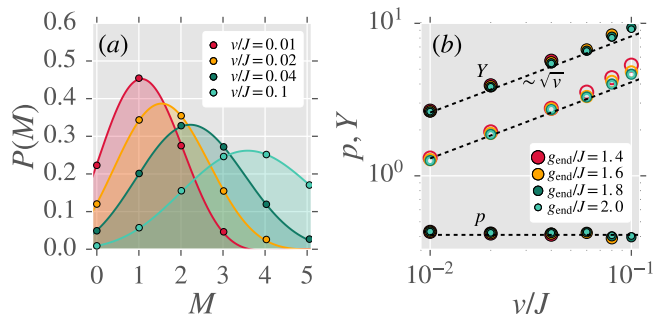


FIG. 3. (a) The distribution $P(M)$ of the number of states at excitation energy $2M(g - J)$ fitted to the pseudo binomial distribution $P(M) = Y!/(Y - M)!/M!p^M(1 - p)^{Y - M}$ ($g_{\text{end}}/J = 2$, $Jt_{\text{wait}} \rightarrow \infty$, different speeds v). (b) Fitted values of p and Y as functions of ramp speed v for different g_{end} . Filled symbols are for $N = 100$ and open ones for $N = 50$ (p for the latter not shown, which are on top of the $N = 100$ data). The data approximately collapses on single lines. Dashed lines show a power-law $Y \sim v^{1/2}$ (with a relative factor of 2 in the prefactor) as well as $p \sim C$.

Panel (b) of Fig. 2 examines in detail the Loschmidt signal at a time corresponding to $g = 1.4J$. Only five states are present with any noticeable weight (the broadening is mainly due to the finite frequency resolution $\Delta\omega$; for details see the SM). The width of the first and second magnon bands are shown as yellow and green bars, respectively; it is clear that the states appearing in the Loschmidt signal sit at or very near to the lowest, zero-momentum energies of these bands; loosely, states with M $k = 0$ magnons. The interpretation of the magnetization in terms of the wave function spectrum is deferred to the SM. In addition, we note at the QCP $g/J = 1$, the decay of $L(\omega)$ follows roughly a strongly decaying power-law $\sim \omega^{-8}$ if the ramp speed is slow (see Fig. 2 (c)).

We find that for g_{end} not too close to 1, the wave function spectrum collapses for different values of g_{end} if the frequency is plotted in units of $2|g_{\text{end}} - J|$ (not shown). It is then useful to define the excitation probability in the bottom ω_M of the M -th magnon band by $P(M) = \frac{1}{2\pi} \int_{\omega_M - 2\Delta\omega}^{\omega_M + 2\Delta\omega} L(\omega) d\omega$. Panel (a) of Fig. 3 shows $P(M)$ for different speeds and demonstrates that the distribution can be fitted perfectly by a binomial form $P(M) = Y!/(Y - M)!/M!p^M(1 - p)^{Y - M}$ with, crucially, a non-integer Y . The defect creation probability p is found to be almost independent of ramp speed v and system size N . Y , which gives the mean number of defects created, scales as the square root of the ramp speed and is linearly proportional to system size, consistent with a constant defect creation density (see Fig. 3 (b)). The $Y \sim \sqrt{v}$ relation is consistent with Kibble-Zurek scaling [5–9], which predicts $pY \sim v^{\frac{d\nu}{1+\nu z}}$, if the known $d = 1$ exponents $z = \nu = 1$ are used. In other words, our analysis demonstrates that the ramp creates quantum defects,

each with independent probability p per unit time and per unit length, with the dependence on the ramp velocity only via the expected value of the number of defects pY . This result goes significantly beyond the standard Kibble-Zurek paradigm.

It is important to keep in mind that Fig. 1 was obtained in the thermodynamic limit $N \rightarrow \infty$, while the wave function spectroscopy can only be performed on finite (yet large) systems. The result that the lowest energy state of each sector is $2M|g - J|$ holds only in the infinite system size limit. In finite systems, these excitations are not at perfect integer multiples of each other [21]. In Fig. 4 (a) and (b), we show a zoom-in of the first two peaks of the wave function spectrum for two different system sizes as well as the exact excitation energies (vertical solid lines) [20–22]. For comparison, dashed lines in (b) show twice the value of the solid lines in (a). Observables such as S^z , which connect eigenfunctions whose magnon numbers M differ by one, thus display a superposition of oscillations at frequencies which are determined by the difference of the energies of the lower edges of two consecutive magnon-bands after the ramp. In case that these oscillation frequencies are very close to each other, one finds a beating signal in S^z and recovers a single oscillation frequency only in the limit $N \rightarrow \infty$ (see Fig. 4 (c)). The position of the first knot in the signal can be estimated analytically (see the SM); the approximated time interval (yellow shaded area in Fig. 4) agrees well with the numerical data. Note that in more generic models, frequency shifts and quantum beats can also be induced by magnon-magnon interactions (in this sense we take finite N as a proxy to more general magnon-magnon interactions found in generic systems). This highlights the importance of the coherence on the dynamics of observables after a sweep through a QCP at finite system size and/or finite magnon-magnon interaction [25]. These results are of direct experimental relevance as current experiments on quantum simulators are performed at sizes of $N \sim 20 - 60$ [26].

Ramp through QCP and back— Finally, we consider the case of two slow ramps, one forward through the QCP as described above and then one backwards, with a finite waiting time t_{wait} in between (see Fig. 5(a)). We focus on the question whether or not the properties after the second ramp (which ends in the original phase that we started with) can be tuned by the time spent in the other phase. As before, the magnetization $S^z(t)$ shows long-lived oscillations after the first ramp but becomes time independent for $t > t_{\text{end}}$ (see Fig. 5 (a)), which one can easily understand from the fact that σ_i^z commutes with H for $g = 0$. In Fig. 5 (b), we demonstrate how the value of the magnetization for $t > t_{\text{end}}$ can be tuned by adjusting the waiting time. One observes that the asymptotic value mimics the oscillations and decay of S^z obtained during the waiting time, and the residual magnetization can hence be frozen in by the second ramp. Even after

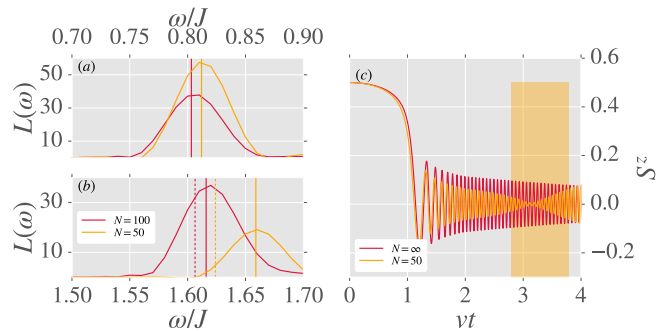


FIG. 4. Finite size dependence of the wavefunction spectrum: Zoom-in of (a) the one magnon as well as (b) the two magnon energy regime. Solid vertical lines shows the exact position of the lowest one or two magnon states. Dashed vertical lines in (b) indicate twice the one-magnon line of (a). (c) Time evolution of the spin expectation value S^z . Wavefunction spectroscopy allows for an analytic estimate for the beat frequency (see SM) and for $N = 50$ from (b) predicts that the first knot of the quantum beat should lie in the yellow shaded region (in agreement with the numerical data). The other parameters are as in Fig. 2 (b).

the second ramp is complete, the defects frozen into the final state approximately follow a Binomial distribution. This is shown for two waiting times in Fig. 5 (c) and is similar to the behavior found after the first ramp (see above). The fit parameters p and Y – and thus the defect distribution – can be controlled by tuning the waiting time. This implies that the phase differences in the pure wave function after the first ramp play an important role for the dynamics of crossing the QCP a second time. We observe that the average number of defects $Y \cdot p$ can be tuned in a range between 1 to 0.75 (inset to Fig. 5 (c)); the fast dependence of $Y \cdot p$ on t_{wait} agrees with the main oscillation $2|g_{\text{end}} - J|$ found during the time when $g > 1$.

Summary and Outlook— We showed that quantum coherence can have prominent consequences for the dynamics encountered after a ramp through a QCP. Most notably, these consequences can manifest in a beating signature of the post-ramp dynamics of a given observable, which can be analyzed by virtue of the wave function spectroscopy we introduced. This tool allows one to interrogate the many-body spectrum of large interacting systems and thus, e.g., characterize magnon-magnon interactions. We also illustrated how coherence in the quantum dynamics affects observables after a second ramp through the same QCP.

The established wave function spectroscopy could yield valuable insights into many other physical situations as well. For example, the extension to infinite temperature calculations (see SM) seems promising to obtain a more complete understanding of the quantum many-body spectrum. Another avenue of future research could include a study of many-body localized systems after a quantum quench, where energy statics are routinely used

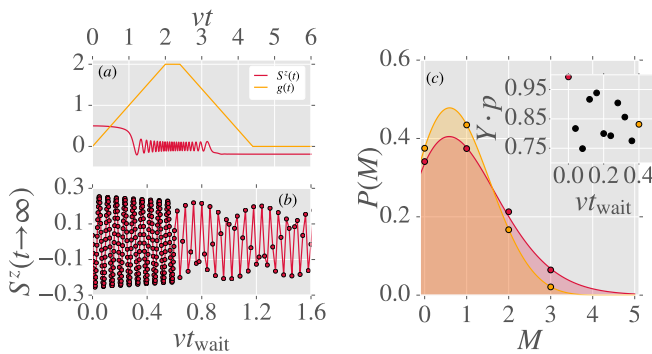


FIG. 5. Results for the double ramp. (a) Dynamics of $S^z(t)$ for a finite $vt_{\text{wait}} = 0.4$ (and $v = 0.02J$, $g_{\text{end}} = 2J$, $N \rightarrow \infty$). After the second ramp is complete, $S^z(t)$ reaches a steady-state value. (b) The asymptotic value of $S^z(t \rightarrow \infty)$ for different waiting times t_{wait} . The other parameters are as in (a). (c) Wavefunction spectrum $L(\omega)$ after the second ramp for two $vt_{\text{wait}} = 0.0$ (red) and $vt_{\text{wait}} = 0.4$ (yellow). The other parameters are the same as in (a), but choosing $N = 100$. Shaded regions show fits to Binomial distributions as in Fig. 3. The inset shows the fitted $Y \cdot p$ in dependency of the waiting time (including more t_{wait} then shown in the main panel), which is the average number of defects.

to classify the mobility edge. At the same time one could apply this tool to obtain a more complete characterization of quantum defects in the fields of quantum computing and counter-diabatic driving.

Acknowledgements. — DMK and CK acknowledge support by the Deutsche Forschungsgemeinschaft through the Emmy Noether program (KA 3360/2-1). AJM was supported by the Basic Energy Sciences Division of the U.S. Department of Energy under grant DE-SC0018218. Simulations were performed with computing resources granted by RWTH Aachen University under projects rwth0013 and prep0010.

<https://doi.org/10.1080/00018732.2010.514702>.

- [10] A. del Campo and W. H. Zurek, International Journal of Modern Physics A **29**, 1430018 (2013), arXiv:1310.1600.
- [11] H. T. Quan and W. H. Zurek, New Journal of Physics **12**, 093025 (2010), arXiv:1007.3294.
- [12] A. Peres, Physical Review A **30**, 1610 (1984).
- [13] H. M. Pastawski, P. R. Levstein, and G. Usaj, Physical Review Letters **75**, 4310 (1995), arXiv:9604019 [cond-mat].
- [14] A. Silva, Physical Review Letters **101**, 120603 (2008), arXiv:0806.4301.
- [15] A. Chenu, J. Molina-Vilaplana, and A. del Campo, (2018), arXiv:1804.09188.
- [16] S. R. White, Physical Review Letters **69**, 2863 (1992).
- [17] G. Vidal, Phys Rev Lett **98**, 70201 (2007).
- [18] U. Schollwöck, Annals of Physics **326**, 96 (2011), arXiv:1008.3477.
- [19] D. M. Kennes and C. Karrasch, Computer Physics Communications **200**, 37 (2016), arXiv:1404.3704.
- [20] E. Lieb, T. Schultz, and D. Mattis, Annals of Physics **16**, 407 (1961).
- [21] P. Pfeuty, Annals of Physics **57**, 79 (1970).
- [22] Y. He and H. Guo, Journal of Statistical Mechanics: Theory and Experiment **2017**, 093101 (2017), arXiv:1707.02400.
- [23] M. Gell-Mann and F. Low, Physical Review **84**, 350 (1951), arXiv:9907483 [hep-ph].
- [24] C. Brouder, G. Stoltz, and G. Panati, Physical Review A - Atomic, Molecular, and Optical Physics **78**, 042102 (2008), arXiv:0807.4218.
- [25] D. M. Kennes, A. de la Torre, A. Ron, D. Hsieh, and A. J. Millis, Phys. Rev. Lett. **120**, 127601 (2018).
- [26] H. Bernien, S. Schwartz, A. Keesling, H. Levine, A. Omran, H. Pichler, S. Choi, A. S. Zibrov, M. Endres, M. Greiner, V. Vuletic, and M. D. Lukin, Nature **551**, 579 (2017), arXiv:1707.04344.
- [27] D. M. Kennes, Physical Review B **96**, 024302 (2017), arXiv:1703.00925.

-
- [1] A. Streltsov, G. Adesso, and M. B. Plenio, Rev. Mod. Phys. **89**, 041003 (2017).
 - [2] R. Mankowsky, M. Först, and A. Cavalleri, Rep. on Prog. in Phys. **79**, 064503 (2016).
 - [3] D. N. Basov, R. D. Averitt, and D. Hsieh, Nature Materials **16**, 1077 (2017).
 - [4] Y. Tokura, M. Kawasaki, and N. Nagaosa, Nature Phys. **13**, 1056 (2017).
 - [5] T. W. Kibble, Journal of Physics A: General Physics **9**, 1387 (1976).
 - [6] T. W. Kibble, Physics Reports **67**, 183 (1980).
 - [7] W. H. Zurek, Nature **317**, 505 (1985), arXiv:9607135 [cond-mat].
 - [8] A. Dutta, G. Aeppli, B. K. Chakrabarti, U. Divakaran, T. F. Rosenbaum, and D. Sen, Quantum Phase Transitions in Transverse Field Spin Models (2015) arXiv:1012.0653.
 - [9] J. Dziarmaga, Advances in Physics **59**, 1063 (2010),

RAMP PROFILE

Here we give the equation describing the time dependent profile of $g(t)$ used in the main text

$$g(t) = \begin{cases} vt & t \in (0, g_{\text{end}}/v] \\ g_{\text{end}} & t \in (g_{\text{end}}/v, g_{\text{end}}/v + t_{\text{wait}}] \\ 2g_{\text{end}} - v(t - t_{\text{wait}}) & t \in (g_{\text{end}}/v + t_{\text{wait}}, 2g_{\text{end}}/v + t_{\text{wait}}) \end{cases}. \quad (3)$$

This ‘double ramp’ is also depicted in the inset to Fig. 1.

DMRG

At time $t = 0$, we prepare one of the ferromagnetic ground states of the model, which for $g(t = 0) = 0$ can be done analytically. We then employ a real time evolution algorithm (see Sect. 7 of Ref. 18) to determine $|\Psi(t^*)\rangle$ via a propagation from $t = 0$ to $t = t^*$ with the time-dependent Hamiltonian $H(t)$; subsequently, $e^{i(H(t^*) - E_0)t^*} |\Psi(t^*)\rangle$ is calculated as a function of t' using a time-independent $H(t^*)$. We employ a fourth-order Suzuki-Trotter decomposition with $J\Delta t = 0.02$ chosen small enough to give converged results [27]. The numerical cost of this method scales in an exponential fashion with the entanglement in the system. The control parameter encoding the entanglement growth (and with it numerical cost) is the so-called bond-dimension. In our simulations the bond dimension is dynamically increased during the real time evolution such that we obtain numerically exact result. For slow ramps the entanglement growth is slow allowing us to perform simulations up to very large times, before the bond-dimension becomes excessively large.

Additionally, we can obtain a trivial factor of two in the achievable time scale [19] for t_{end} by calculating the norm of the state $|\Psi'\rangle = e^{i(H - E_0)t'/2} |\Psi(t^*)\rangle$ instead of the overlap of $e^{i(H - E_0)t'} |\Psi(t^*)\rangle$ with $|\Psi(t^*)\rangle$.

FINITE TEMPERATURE GENERALIZATION

It is straightforward to extend the presented ideas to nonzero temperature. Let us assume we have a canonical ensemble

$$\rho = e^{-\beta H} / Z. \quad (4)$$

The generalization of the wavefunction spectrum

$$L(t') = \frac{1}{Z} \text{Tr} \left[e^{-i(H - E_0)t'} \rho \right] = \sum_n e^{-\beta E_n - i(E_n - E_0)t'} \quad (5)$$

now yields the Fourier transform

$$L(\omega) = \frac{C}{Z} \sum_n e^{-\beta E_n} \delta(\omega - (E_n - E_0)) \stackrel{E_n \text{ dense}}{=} e^{-\beta \omega} \rho(\omega). \quad (6)$$

The $\beta \rightarrow 0$ limit thus allows to access the state density $\rho(\omega)$ directly. This is an important quantity and it can, e.g., be used to identify gaps in the many-body spectrum or tell us about the distribution of eigenenergies (as is often used to classify many-body localized systems). The $\beta > 0$ case allows to analyze where in the spectrum of H the energy is distributed and allows to analyze how thermal a state looks after, e.g., a quench or ramp by a rigorous comparison of the entire spectrum.

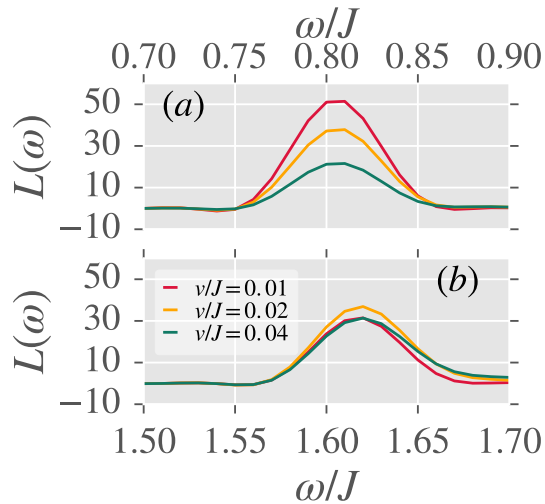


FIG. 6. (a) and (b) Wavefunction spectrum $L(\omega)$ around frequencies corresponding to Δ and 2Δ for $g_{\text{end}}/J = 1.4$, $Jt_{\text{wait}} \rightarrow \infty$ and different speeds v .

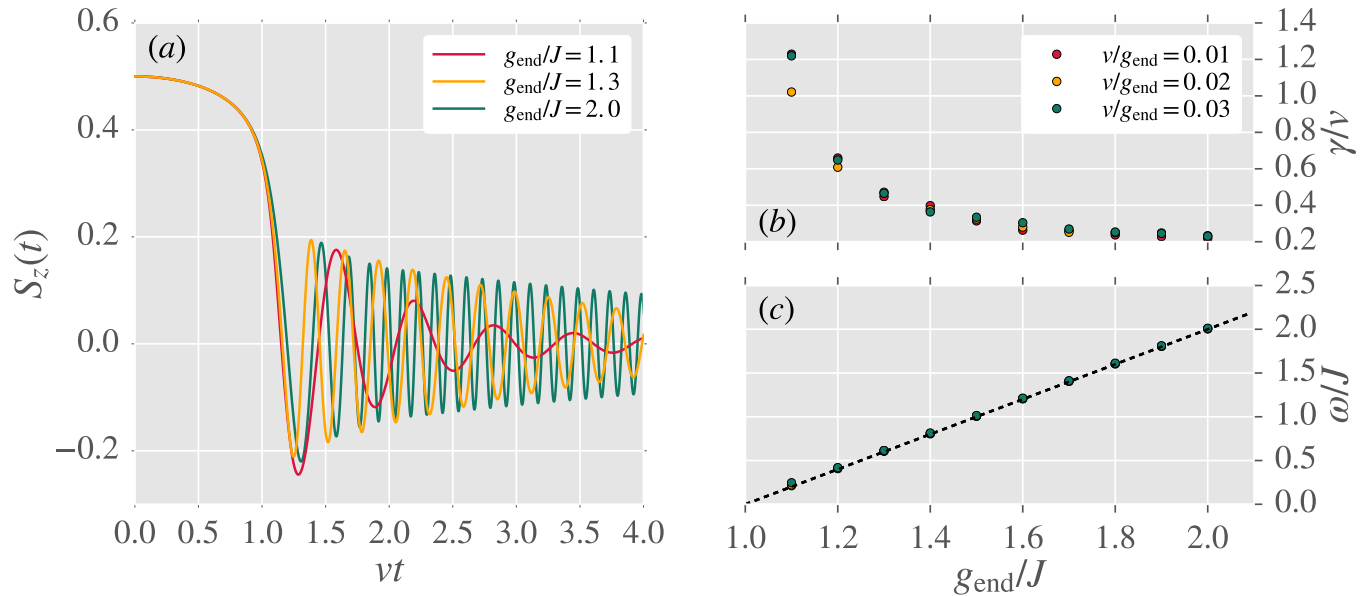


FIG. 7. (a) Dynamics of $S^z(t)$ for different g_{end} and $v = 0.01g_{\text{end}}$, $t_{\text{wait}} \rightarrow \infty$ and $N \rightarrow \infty$. The dynamics at large times fit well to a damped harmonic oscillation $C \exp(-\gamma t) \sin(\omega t + \delta)$. (b) and (c) show the fitted parameters γ and ω in dependence of g_{end} . In (c) the dashed black line is the function $f(x) = 2|g_{\text{end}} - J|$.

OBSERVABLES FROM WAVEFUNCTION SPECTROSCOPY

Here we analyze the wave function spectrum in more detail and connect to results obtained by the Kibble-Zurek intuition. We observe that the nonequilibrium probe $g(t)$ (being spatially uniform) can only create states of total momentum $k = 0$. In the one spin-flip sector, the only such state is the minimum energy magnon. In the multi-spin-flip sectors, there is a continuum of states with zero total momentum. However, while present in principle, the ‘multi-magnon continuum’ in practice makes a remarkably small contribution. To see this we present in panels (a) and (b) of Fig. 6 an expanded view of the Loschmidt peaks in the one- and two-spin flip sectors for different ramp speeds. The one-magnon peak is symmetric, with width given solely by the frequency resolution. In the two spin flip sector the fastest ramp shows a weak asymmetry, with slightly more weight on the high energy side; This means that for not too slow ramps a small density of “ k plus $-k$ ” two-magnon excitations are created, whose density can be

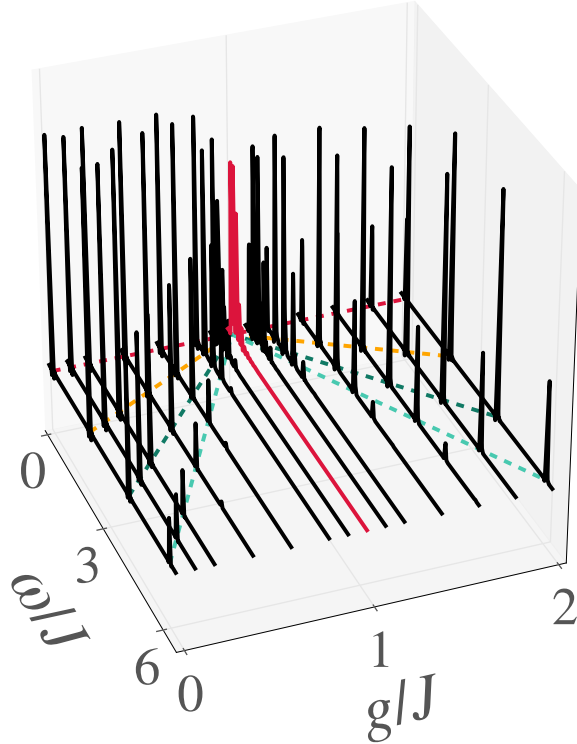


FIG. 8. Wavefunction spectrum $L(\omega)$ during the second (backward) part of the ramp at times parametrized by $g(t) = g$ taking the second time $g(t)$ reaches g . $vt_{\text{wait}} = 0.0$ and the other parameters are as in Fig. 5. The gap excitation energy $\omega = 2|g - J|m$ is given as colored dashed lines. The slice for $g_{\text{stop}} = g_c = 1$ is highlighted in red.

controlled by the speed of the ramp.

In order to interpret the magnetization oscillations in terms of these findings, we express $S^z(t)$ in the eigenstates $|\{k_j, m_j\}\rangle$ of $H(t > t_{\text{end}})$:

$$S^z(t) = \sum_{\{k_j, m_j, m_l, k_l\}} a_{\{k_j, m_j\}}^* a_{\{k_l, m_l\}} e^{i(E_{\{k_j, m_j\}} - E_{\{k_l, m_l\}})t} \langle \{k_j, m_j\} | \sum_i \sigma_i^z | \{k_l, m_l\} \rangle. \quad (7)$$

If a continuum of states were important, then the different terms in the sum would dephase, leading to an exponential decay of $S^z(t)$. However, the Loschmidt analysis shows that the only states that contribute are a small number of zero-momentum states precisely at the bottoms of the few-magnon bands. Therefore, the dominant contribution is the single state that is at the bottom of each m -magnon band. Including only this contribution we can replace the sum over all m -magnon states $\{m\}$ in Eq. (7) by a sum only on the lowest-lying states ($k = 0$), obtaining

$$S^z(t) = \sum_{m, m'} a_{m, k=0} a_{m', k'=0} e^{i(E_{m, k=0} - E_{m', k=0})t} \langle m, k=0 | \sum_i \sigma_i^z | m', k'=0 \rangle \quad (8)$$

We can view the bottom of the magnon band states as quantum defects in the wave function, induced by the ramp. The energy spacings between these are integer multiples of $2|g_{\text{end}} - J|$ (compare Fig. 2 (b)). Noting that in the given

basis, σ_i^z is the product of sums of raising and lowering operators on adjacent sites and thus connects eigenfunction whose total magnon numbers M differ by one, this directly explains the oscillations with frequency $2|g - J|$ depicted in Fig. 1. The density of these quantum defects in the ground-state wave function (coherent superposition of higher-excited states) can be read off by determining their density $\sim |a_m|^2$, which are the height of the peaks in the wave function spectrum $L(\omega)$.

ESTIMATION OF BEAT FREQUENCY FROM FINITE SIZE

From the frequency difference found in the wave function spectrum at finite N , we can estimate the first knot in the signal due to the beating in the signal. Taking $N = 50$ and concentrating only on the three lowest magnon-bands, which captures most of the weight of the wave function after performing a ramp as considered in Fig. 4, a knot should appear around times $\Delta t = t_0 + \pi/(|\Delta E_{\text{magnon}}^1 - \Delta E_{\text{magnon}}^0|)$, where t_0 has to be estimated somewhere between the time where the ramp crosses the QCP and the time it is completed. In more generic situation where magnons interact a similar estimate should be possible.

ADDITIONAL DATA FOR $S^z(t)$

The oscillatory dynamics in $S^z(t)$ are superimposed by a dephasing mechanism which stems from the finite width of the wavefunction spectrum. To disentangle the beating phenomena identified at finite N in the main text from the dephasing we next concentrate on the dynamics as $N \rightarrow \infty$. The wavefunction spectrum would suggest that at $N \rightarrow \infty$ the differences in energy of the lower m -magnon bands align perfectly giving rise to a dominant frequency of $\Omega = 2|g - J|$ in the dynamics of S^z . The damping of these dynamics at least at g not too close to 1 via dephasing is given by the width in energy of the m -magnon peaks themselves, which reduces as the ramp speed is lowered. Indeed all of these prediction from the wavefunction spectrum are confirmed in the dynamics as depicted in Fig. 7. The dephasing is found to scale linearly in v such that quantum coherence in the wavefunction can be observed on ever larger time scales as the ramp is made slower (compare Fig. 7 (b)).

WAVEFUNCTION SPECTRUM DURING THE DOUBLE RAMP

Fig. 8 shows the wavefunction spectrum during the time t of the backward ramp parametrized by $g(t) = g$ for the second part of the ramp for the same parameters as in Fig. 5.
